PUBLICATIONS OF THE ASTRONOMICAL SOCIETY OF THE PACIFIC, **113**:105–118, 2001 January

PHARO: A Near-Infrared Camera for the Palomar Adaptive Optics System

T. L. HAYWARD,[1] B. BRANDL, B. PIRGER, C. BLACKEN, G. E. GULL, J. SCHOENWALD, AND J. R. HOUCK

Center for Radiophysics and Space Research, Cornell University, Ithaca, NY 14853

Received 2000 May 28; accepted 2000 September 8

ABSTRACT. We describe Cornell's near-infrared camera system PHARO (Palomar High Angular Resolution Observer) built for use with the JPL Palomar Adaptive Optics System on the 5 m Hale telescope. PHARO uses a 1024 × 1024 HgCdTe HAWAII detector for observations between 1 and 2.5 μm wavelength. An all-reflecting optical system provides diffraction-limited images at two scales, 25 and 40 mas pixel^{-1}, plus a pupil imaging mode. PHARO also has a coronagraphic imaging capability and a long-slit grism spectroscopy mode at resolving power ≈1500. The instrument has been in use with the AO system at Palomar since early 1998.

1. INTRODUCTION

The introduction of adaptive optics (AO) systems at several observatories is a significant recent advance in ground-based astronomy. AO systems, by adaptively correcting optical wavefront errors induced by atmospheric turbulence, allow large telescopes to achieve nearly diffraction-limited performance at near-infrared (NIR) wavelengths. The average seeing at a typical observatory is of the order of 1″, while the diffraction limit in the NIR is ≲100 mas for 4 m class or larger telescopes, so the potential performance gain is large. Thus, AO systems have become an important design feature of nearly all large telescopes currently in operation or under construction.

The 5 m Hale telescope at Palomar Observatory is one of the facilities for which an AO system has been developed. The Palomar AO project was undertaken as part of a collaborative agreement between the California Institute of Technology and the NASA Jet Propulsion Laboratory (JPL), which provides JPL observers with access to the 5 m telescope in return for assistance with supporting the facility, partly in the form of the construction of new facility instrumentation. In 1994 the Spatial Interferometry Systems Group at JPL proposed to build an advanced AO system that would allow the 5 m to perform near the diffraction limit in the NIR, between $\lambda = 1$ and 2.5 μm. Development of the Palomar system started shortly thereafter.

Also in 1994, the astronomy department at Cornell University, which had just renewed a similar cooperative agreement with Caltech, was considering options for its next Palomar instrument. We realized that the forthcoming AO system would benefit from a specialized camera. Existing Palomar infrared instruments would not sufficiently sample the diffraction-limited point-spread function (PSF), dictating a fresh optical design. We therefore decided to build a dedicated NIR camera in support of JPL's AO effort. The camera was named the "Palomar High Angular Resolution Observer," or PHARO.

This paper describes the design and development of PHARO and presents first results from the common system. A previous description of the design was given by Brandl et al. (1997). The AO system itself has been described by Dekany et al. (1998) and Troy et al. (2000), so it will be only briefly summarized here.

2. INSTRUMENT DESIGN

The anticipated performance of the Palomar AO system sets the boundary conditions for our camera design. The primary goal, of course, is to sample the diffraction-limited PSF, which is typically an order of magnitude smaller than the average seeing disk on Palomar.

2.1. Imaging through the Atmosphere

Practically, the quality of the PSF delivered by an AO system depends not only on wavelength λ and telescope diameter D but also on the atmospheric conditions. The theory of imaging through atmospheric turbulence is described in several recent works (e.g., Tyson 1998; Hardy 1998; Roddier 1999; Schroeder 2000). Two important quantities which are commonly used to characterize the atmosphere are the so-called coherence length r_0 (also called the Fried parameter), which is essentially the size of a turbulence cell over the telescope at a given wavelength, and the coherence time τ. The r_0 parameter is proportional to $\lambda^{6/5}$, and 1″ visible seeing corresponds to $r_0 \approx 10$ cm. As r_0 decreases, the seeing worsens, and more active elements within the AO control loop are required to flatten the incoming wave front. The time constant τ_0 over which the atmospheric turbulence is quasi-static sets the minimum bandwidth for the correction loop. Most current AO systems measure the wave front at visible wavelengths with low read noise CCD detectors and record the scientific data at NIR wavelengths where the

[1] Current address: Gemini Observatory, Casilla 603, La Serena, Chile; thayward@gemini.edu.

TABLE 1
AO System Capabilities

Band	λ (μm)	Diffraction FWHM (mas)	Maximum Strehl Ratio[a]	Guide Star $V = 12$ Strehl Ratio[b]	Isoplanatic Angle (arcsec)
J	1.25	48.9	0.20	0.02	25
H	1.65	64.5	0.41	0.05	34
K	2.20	86.0	0.63	0.12	50

Note.—Strehl ratios and isoplanatic angles are dependent on many factors, so the quoted values are approximate.

[a] For a $V < 7$ guide star in less than 1″ visible seeing.

[b] For a $V \approx 12$ guide star in 1″ visible seeing.

absolute requirements on the wave-front correction are less stringent.

The quality of the corrected image can be characterized by the Strehl ratio, defined as the ratio of the peak flux of an observed point-source image to the theoretical peak flux in a diffraction-limited PSF at that telescope. A perfect diffraction-limited image therefore has a Strehl ratio of 1.0, while an astronomical image degraded by seeing may have a Strehl ratio $\ll 0.1$. An AO system increases the Strehl ratio by concentrating some fraction of the total signal into a sharp, almost diffraction-limited core. Because AO systems do not correct the image completely, however, some of the light is spread into a large, diffuse halo, producing the so-called core-halo distribution. The point-source sensitivity of an AO camera is therefore highly dependent on the Strehl ratio that can be achieved under the existing seeing conditions at the desired wavelength. In addition, high Strehl ratio can be achieved only within a rather small patch on the sky, the so-called isoplanatic angle Θ_0. The error in the wave-front correction increases with increasing angular separation from the reference star as $\sigma^2 \approx (\Theta/\Theta_0)^{5/3}$, as more and more light passes through unsampled turbulence cells. The isoplanatic angle also depends on the wavelength.

2.2. The Palomar AO System

The maximum Strehl ratio that can be achieved by an AO system at a certain wavelength under given atmospheric conditions is governed by a few fundamental parameters of the hardware. The Palomar AO system (Troy et al. 2000) is based on a Shack-Hartmann wave-front sensor (WFS), which divides the telescope entrance pupil (the primary mirror) into a rectangular grid, and a deformable mirror (DM) with adaptive elements also laid out in a corresponding grid. To sample the wave front sufficiently, the spacing of the WFS grid and DM adaptive elements should be less than r_0 at the science wavelength, and the maximum stroke of the elements should be sufficient to remove the largest wave-front errors. The bandwidth of the system should be higher than $1/\tau_0$ for maximum correction. The bandwidth is limited not only by the response time of the adaptive optical elements but also by the brightness of available guide stars and the sensitivity of the wave-front sensor camera.

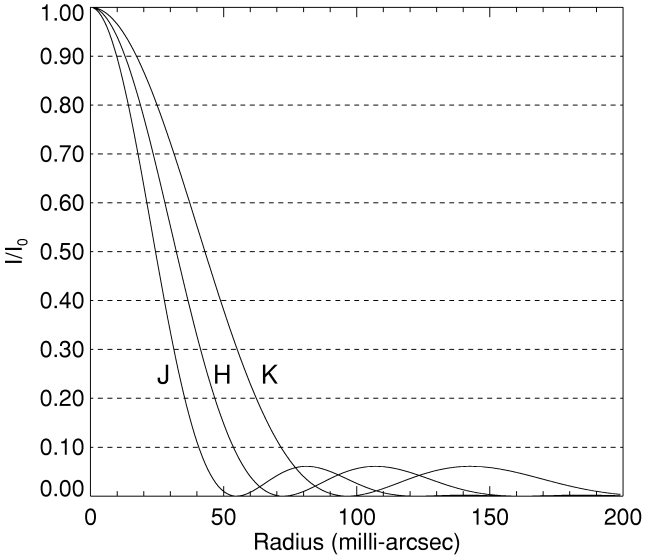

Fig. 1.—Intensity profiles of the Hale telescope's diffraction-limited PSF at *J*, *H*, and *K*. The clear aperture is 5.093 m, and the central obscuration diameter is 1.829 m. The FWHM is $0.963\lambda/D$ radians, or 48.9 mas at *J*, 64.5 mas at *H*, and 86.0 mas at *K*.

The Palomar system uses a DM built by Xinetics, Inc., which contains 349 lead magnesium niobate (PMN) actuators. The actuators deliver a mechanical stroke of 4 μm, with a maximum permissible stroke difference between adjacent actuators of 1 μm. The DM area which corresponds to the primary mirror is 17 actuators in diameter and contains a total of 241 elements. The DM is reimaged onto a 16 × 16 lenslet array, which in turn feeds a WFS camera based on a 64 × 64 pixel, low read noise (~6 e^-) CCD from MIT/Lincoln Labs. Therefore, 4 × 4 pixels per lenslet are used to compute image centroids. The WFS currently has a maximum readout frequency of 500 Hz, the DM bandwidth is 20 Hz (−3 dB), and the tip-tilt bandwidth is 5 Hz (−3 dB). JPL is currently pursuing an upgrade plan to increase these closed-loop bandwidths.

The measured performance of the Palomar AO system is summarized in Table 1. At present, the system requires natural guide stars for wave-front sensing. Some of the tabulated values represent ~1″ visible seeing, about average for Palomar. Under these conditions, the AO system can achieve very high Strehl ratio at *K* and a significant correction at *J*. The isoplanatic angle values were determined from images of the open cluster NGC 6871 by Marshall et al. (2000). The angle is somewhat larger than predicted by theory, indicating that the altitude h_0 of the dominant seeing layer is less than 1 km, similar to the findings at Mauna Kea observatories (Roddier 1999, p. 50).

2.3. PHARO Optical System

The expected performance of the AO system led directly to several fundamental specifications for PHARO. Figure 1 illus-

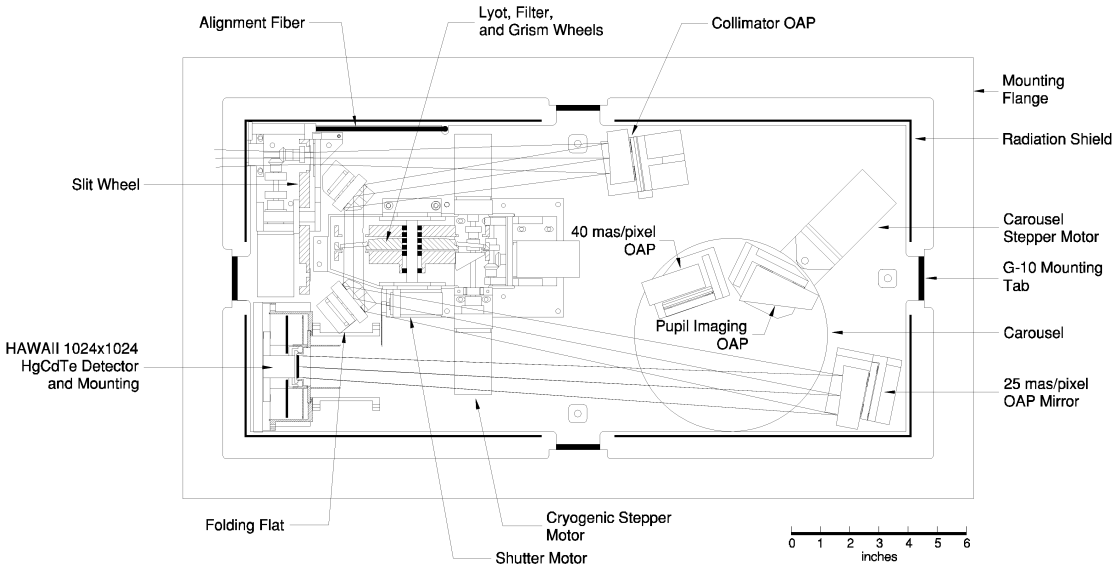

FIG. 2.—PHARO optical design. The instrument is shown in the f/30 (25 mas pixel^{-1}) imaging configuration. Several covers and light baffles are omitted for clarity.

trates the diffraction-limited PSF profiles at *J*, *H*, and *K* for the Hale telescope, taking into account the 1.83 m central obscuration (Born & Wolf 1980, p. 416). The FWHM of the PSF equals $0.963\lambda/D$ radians, or as small as 48.9 mas at *J*. Therefore, the AO system's ability to deliver images near the diffraction limit dictated that PHARO's pixels subtend no more than 25 mas in order to sample the images properly. At this scale, the 1024 × 1024 infrared arrays that were becoming available in the mid-1990s cover a large portion of the isoplanatic patch, making them the obvious choice for our instrument. The HgCdTe "HAWAII" array made by the Rockwell Science Center is especially well suited for our application because of its small 18.5 μm pixel pitch. The scale of the f/15.64 beam provided by the AO system is 48 mas over 18.5 μm, so only moderate magnification is required in the camera to reach the desired sampling. The small pitch also minimizes the size of the optical system and therefore the size and cost of the entire instrument. The standard HgCdTe array is most sensitive between $\lambda \approx 1$ and 2.5 μm, the wavelength range over which the AO system is most effective.

TABLE 2
OPTICAL DESIGN PARAMETERS

Parameter	Value
f/15.64 image scale (arcsec mm^{-1})	2.584
f/18.69 image scale (mas pixel^{-1})	39.91
f/29.91 image scale (mas pixel^{-1})	25.10
Pupil diameter (mm)	16.88
Collimator OAP focal length (mm)	254.0
f/18.69 Camera OAP focal length (mm)	303.4
f/29.91 Camera OAP focal length (mm)	485.6
Pupil imaging focal length (mm)	203.4
Pupil imaging conic constant	−0.060

PHARO's optical design was optimized to provide diffraction-limited image quality over the expected isoplanatic field at $\lambda = 2.2$ μm. High throughput and freedom from ghosts and scattered light were important design goals because we expected that imaging of faint sources near bright stars, which requires the highest possible image contrast, would be a major application of the camera. Two choices that relaxed the demands on the optics were to limit the field size to a relatively modest 30″–40″, sufficient to cover the isoplanatic field, and not to require extremely high image quality over the entire field because in most cases the limiting factor would be the anisoplanatism. The instrument design was also constrained by the restricted volume reserved for PHARO on the AO system optical bench and the desire to maximize stiffness of the optics relative to the AO system. Because the system is mounted at Cassegrain focus, its operating angle varies, and it is important to minimize image and pupil motion due to flexure through a wide range of zenith angles.

These design goals led to a simple, all-reflecting optical system. The optical layout is illustrated in Figure 2, and Table 2 lists the important parameters of the design. The optics are based on off-axis paraboloid (OAP) mirrors which reimage the AO focal plane onto the detector. The first OAP collimates the incoming beam and images the pupil onto a cold Lyot stop. The second, "camera," OAP refocuses the collimated beam onto the detector. The entire optical path lies in a single plane, and two flat mirrors fold the beam so the entire system fits into an acceptable envelope. We found that we could accommodate two camera mirrors working at f/30 and f/19. The f/30 mirror

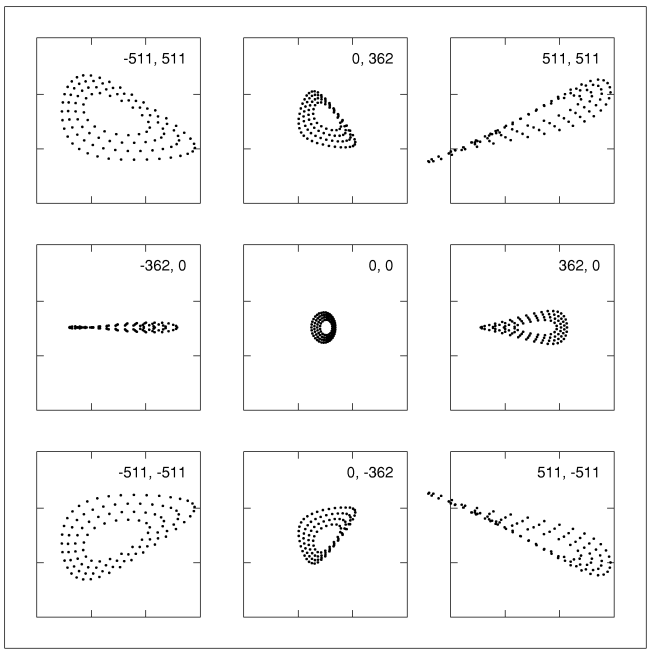

Fig. 3*a*

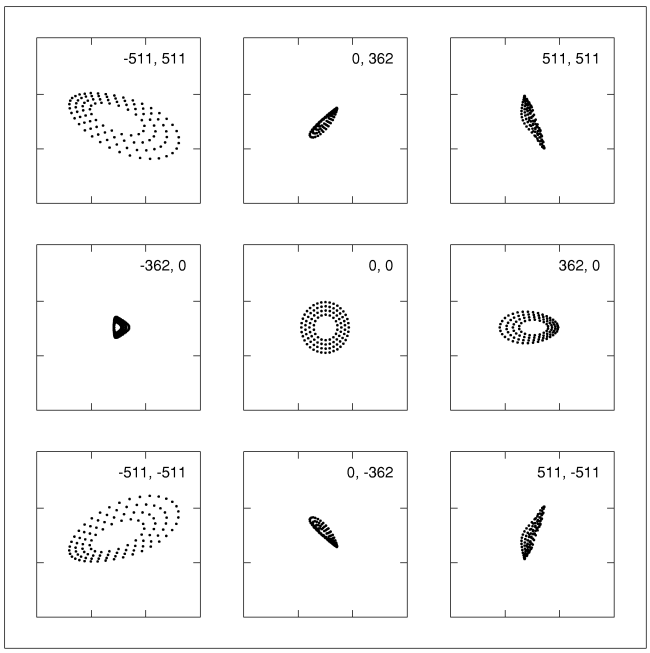

Fig. 3*b*

FIG. 3.—Geometric spot diagrams for PHARO. (*a*) f/30 mode, (*b*) f/19 mode. Each small box is 3 × 3 pixels in size and is labeled with the *x*, *y* offset from the center of the detector in pixels. Since an all-reflective system is achromatic, no significant change with wavelength is noticeable as long as diffraction is neglected.

is fixed and provides 25 mas pixel^{-1} for better sampling of the PSF at *J*. The f/19 mirror can be rotated into the beam to provide 40 mas pixel^{-1}, which still critically samples the PSF at *K* and improves coverage of the isoplanatic patch at *K* in good seeing.

The PHARO optical design was optimized using the ZEMAX ray-trace program. Figure 3 shows a series of spot diagrams for the f/30 and f/19 imaging modes. Both modes provide a Strehl ratio greater than 80% (diffraction-limited performance) over the entire field of view and greater than 95% out to the middle of each edge of the array. Image distortion is an aberration which cannot be completely eliminated in our simple system but is rather small: the maximum distortion is 0.40% in the f/30 mode and 0.84% in the f/19 mode.

TABLE 3
SLIT WHEEL

Number	Name	Comment
1	0.″43 coronagraph spot	5 Airy rings at 2.2 μm
2	0.″13 slit	$R \sim 1500$ spectroscopy
3	0.″97 coronagraph spot	11 Airy rings at 2.2 μm
4	0.″26 slit	$R \sim 750$ spectroscopy
5	Pinhole grid	Optical testing
6	0.″52 slit	$R \sim 375$ spectroscopy
7	40″ field mask	Standard imaging
8	Spare slit	
9	25″ field mask	Standard imaging
10	2″ occulting bar	Imaging

The f/30 and f/19 mode optical axes are not perpendicular to the detector plane in this simple design but are tilted by 0.°1 for f/30 and 0.°7 for f/19. For geometrical reasons, a pixel scale above 40 mas would increase the tilt angle and unacceptably degrade the image quality at the edges of the detector. The f/30 camera mirror focal length is the longest that can be accommodated given the limits on the dewar size.

The telescope+AO+PHARO system has three pupils within the imaging path: the telescope primary mirror, the deformable mirror, and the camera stop. The alignment of the pupils is critical for minimization of background and scattered light as well as maximization of throughput, so we incorporated a third imaging mode into our design that allows direct imaging of the overlapping pupils onto the detector. Since the pupil imaging optics need not be diffraction limited, just oneoptical element, a third off-axis mirror with a conic constant $c \approx -0.05$, provides sufficient image quality. This element is mounted on the carousel together with the 40 mas pixel^{-1} OAP so that it can be inserted in the beam as desired.

The all-reflecting design is free from the ghosts that arise in a lens-based design and by default is also free from chromatic aberration. In addition, the OAPs are constructed of the same aluminum material as their mounts and the other mechanical pieces of the dewar, ensuring that optical alignment will be maintained when the instrument is cooled to operating temperature.

TABLE 4
LYOT WHEEL

Number	Name	Dimensions[a] (mm)	Comment
1	Block		Cold block
2	Open		Open hole
3	Standard cross	6.1, 16.5, 0.25	Standard pupil and spider mask
4	45° cross	6.1, 16.5, 0.25	Second standard mask rotated 45°
5	Medium cross	7.6, 15.4, 0.83	Over/undersize cross for coronagraphy
6	Large cross	9.4, 13.5, 1.75	Over/undersize cross for coronagraphy
7	Standard spot	6.1, 16.5	Central obscuration mask without spiders
8	Spare 1		
9	Spare 2		
10	Spare 3		

[a] Central obscuration diameter, outer diameter, and spider thickness, respectively. The pupil diameter is 16.88 mm and the telescope central obscuration corresponds to 6.08 mm.

TABLE 5
FILTER WHEEL

Number	Name	Central λ (μm)	Bandpass (μm)	Peak Transmission (%)	Manufacturer
1	Open	...	...	...	
2	*J*	1.246	0.162	87	OCLI
3	*H*	1.635	0.296	85	OCLI
4	*K*	2.196	0.336	90	OCLI
5	*K′*	2.121	0.351	92	OCLI
6	K_s	2.145	0.310	92	OCLI
7	Brγ	2.166	0.02	75	Barr
8	H_2 2–1	2.248	0.02	68	Barr
9	CO bandhead	2.295	0.02	72	Barr
10	*K* continuum	2.26	0.06	83	Barr

The four OAP mirrors in PHARO are diamond-turned aluminum made by Lumonics Optics (Nepean, Ontario, Canada). According to the manufacturer's interferometric measurements, the average mirror surface figure quality at 633 nm is λ/12.4 peak to valley (P-V) and λ/77 rms, better than the specification of P-V < λ/8. The two folding mirrors were made from Zerodur polished to λ/20 P-V surface quality by Janos Technology, Inc. The resulting wave-front error from four reflections at two OAPs and two flats is λ/7 P-V at 1.25 μm, corresponding to an rms wave-front error of only 35 nm. All mirror surfaces are coated with protected gold.

2.4. Filters and Grisms

PHARO contains a 10 position wheel at the image plane just inside the dewar window which carries a selection of field stops, slits, coronagraphic masks, and a pinhole mask for image quality checks. Three more 10 position wheels are located between the folding flats. The first of these wheels lies at the pupil plane and contains a set of cold Lyot-stop masks. The pupil diameter is 16.12 mm to accommodate standard 25 mm diameter filters. The second and third wheels carry filters for imaging and grisms for spectroscopy.

Tables 3–7 list the elements currently installed in the four wheels. The five broadband filters in PHARO (*J*, *H*, *K*, *K′*, K_s) were manufactured by OCLI especially for and according to the specifications given by the Gemini filter consortium with tight constraints on the average transmission (>80%), substrate flatness [<0.0183 × λ/(n − 1)], and surface parallelness (<5″). In addition, the filters are expressly designed to be operated at a tilt of 5°. The camera also currently contains narrowband filters manufactured by Barr Associates and NDC Infrared Engineering (United Kingdom) for imaging in five spectral lines and two neutral density (ND) filters with optical densities of 2 and 3 to allow the observation of brighter targets. All filters are mounted at a 5° tilt angle, which is slightly more than the 3° needed to avoid ghosts between filter surfaces according to our analysis.

PHARO includes a long-slit spectroscopic capability to enable high angular resolution spectroscopy of AO targets. The large detector format allows the very attractive mode of dispersing an entire near-infrared (*J*, *H*, or *K*) band across the 1024 pixels at resolving power $R = \lambda/\Delta\lambda \approx 1200$–$1500$ to permit detection of faint spectral features even in the presence of bright continuum emission. The narrow 130 mas slit used to achieve this resolution helps to isolate sources from neighboring objects and minimizes background emission.

The spectroscopy mode was implemented by mounting three grisms in the second filter wheel. The grisms work in the first order of diffraction and disperse the *J*, *H*, and *K* bands, respectively, across the full width of the detector with the instrument in the 40 mas pixel^{-1} mode. The broadband filters in the first filter wheel provide order sorting. We chose the Ohara glasses S-TIH10, with refractive index $n(2\ \mu\text{m}) \approx 1.69$, for the *H*- and *K*-band grisms, and S-LAH60, with $n(2\ \mu\text{m}) \approx 1.79$, for the *J*-band grism. The indices of these glasses are a good compromise between the high index needed to minimize the blaze angle and the lower index desired to match the index of the grating resin ($n \approx 1.59$) and minimize reflection losses at the boundary layer between the prism and the grating. Details of the grism designs are listed in Table 7. The prisms were manufactured from Ohara blanks by J.A. Optics (Utica, New York), and the gratings were replicated from custom-made masters by Diffraction Products (Woodstock, Illinois). Three slits of widths 50, 100, and 200 μm (130, 260, and 520 mas), manufactured by Deerfield Optics (Framingham, Massachusetts), are mounted in the slit wheel for the spectroscopy mode. The spectral resolution of PHARO is primarily limited by the number of resolution elements across the detector, and thus the narrowest slit (50 μm, 130 mas) provides the highest resolution, $R \approx 1500$.

TABLE 6
GRISM WHEEL

Number	Name	Central λ (μm)	Bandpass (μm)	Peak Transmission (%)	Manufacturer
1	ND-1	...	...	1	Janos
2	*H* Grism	...	...	...	
3	Open	...	...	...	
4	*K* Grism	...	...	...	
5	[Fe II]	1.648	0.030	65	Barr
6	*H* continuum	1.668	0.018	65	Barr
7	Open	...	...	...	
8	Paβ	1.272	0.024	62	Barr
9	*J* Grism	...	...	...	
10	ND-2	...	...	0.1	Janos

A drawback of this simple spectrograph design is that the incoming beam does not pass through a cold pupil stop before suffering diffraction at the slit edges, making the camera pupil ill defined. However, adding an additional stage to the optics before the slit would have introduced unacceptable complexity into our design and degraded the performance of the camera modes, so we chose to accept the slightly higher background and less throughput in our spectral mode.

2.5. Coronagraph Mode

Because of its initial reliance on natural guide stars, we expect that a significant scientific application of the Palomar AO system and PHARO will be to search for and study faint companions to bright stars. To facilitate such studies, PHARO includes a coronagraphic capability which utilizes two occulting spots in the slit wheel with diameters of 0.″43 and 0.″97, corresponding to five and 11 Airy rings at 2.2 μm, respectively. The occulting masks are aluminum spots with an optical density of 5 on a CaF_2 substrate, manufactured by Gurley Precision Instruments (Troy, New York). In order to maximize the image contrast in the coronagraphic mode by blocking the diffracted light, special stops are provided in the Lyot wheel (at the pupil plane) that are 76% and 40% of the aperture area in size (see Table 4).

2.6. Cold Shutter and Alignment Fiber

We also incorporated a cold shutter into PHARO, which is desirable for two reasons:

1. The minimum exposure time for the entire detector is limited to ~1 s by the readout. A fast shutter can provide shorter integration times, avoiding saturation due to bright objects as well as offering the possibility of studying seeing characteristics in AO open-loop mode.
2. The correction efficiency of the AO system might vary during long integrations. The AO system can command the shutter to close temporarily during periods of poor correction, eliminating the need to read and reset the detector before an optimal integration time (to achieve background-limited performance, for example) is achieved.

The shutter is implemented by a simple blade mounted just after the second folding flat, close enough to the pupil to minimize differential integration time effects across the field of view. The blade is mounted on the shaft of a cryogenic stepper motor and can be opened or closed in about 0.1 s. The motors used in PHARO are described further in § 3.2.

We realized that even with a very stiff mechanical design, accurately centering a point source in a 50 μm wide slit over a long period of time through varying zenith angle is a challenging task. All optical and optomechanical components behind the AO system's dichroic beam splitter are not part of the adaptively corrected common path and may be sources of small but significant flexure. We therefore decided to place an alignment light source within the camera dewar, to provide the AO system with a reference target so that small flexures can be detected and corrected by the AO system in real time.

The alignment light source is a 50 μm monomode fiber that runs from a vacuum-sealed SMA connector in the dewar wall to a mounting block at the focal plane next to the slit wheel. The SMA connector accepts light from an external laser source, and the fiber emits light through a small BK-7 window mounted next to the main camera window. The laser beam travels back through the AO optical path until it is intercepted by a small pickoff mirror and directed to a sensor (Bloemhof & Dekany 1998, 1999).

2.7. Additional Features

Since the optical system consists mostly of reflective elements, ghost images are minimal. However, reflections can occur within or between the dewar window, the filters, the

TABLE 7
GRISMS

Grism	Wavelength Range (μm)	Dispersion (nm pixel^{-1})	Prism Material	Apex Angle (deg)	Grating at 77 K (lines mm^{-1})	*R* with 0.″13 Slit
J	1.17–1.33	0.15771	Ohara S-LAH60	30.05	322.7	1850–2110
H	1.49–1.78	0.28467	Ohara S-TIH10	25.78	183.9	1310–1550
K	2.03–2.37	0.33215	Ohara S-TIH10	28.89	149.7	1690–1970

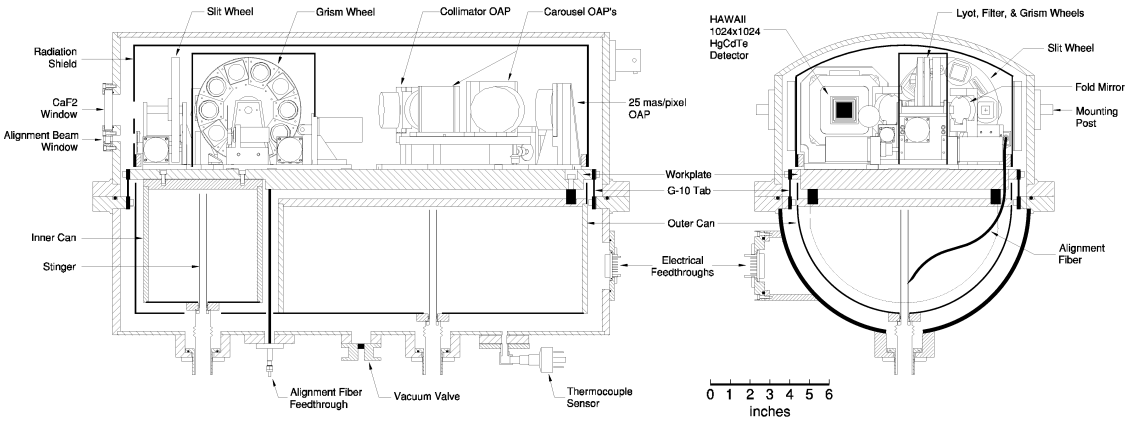

FIG. 4.—PHARO dewar design. Several covers and light baffles are omitted for clarity.

substrates for the masks, and the detector surface. To minimize reflections and increase throughput, therefore, the window and mask substrates made of CaF_2 have been antireflection coated by Janos, providing an average two-surface transmission of 98% between 1.0 and 2.5 μm. Because the camera window is 3 inches (7.6 cm) in front of the AO focus, dust particles on the outer window surface will be blurred to $\sim\frac{1}{3}$ of the field size, avoiding sharp "artifacts." The total sag of the CaF_2 window due to the pressure difference has been calculated to be less than 0.25 μm, with no effect on image quality.

3. MECHANICAL CONSTRUCTION

3.1. Optomechanics

PHARO's mechanical design was developed in-house at Cornell using AutoCAD software. The ray traces from ZEMAX were imported directly into the AutoCAD drawings, resulting in a very precise specification of the positions of the optical elements. Nearly all of PHARO's mechanical components are constructed of 6061-T6 aluminum to minimize differential contraction upon cooling; critical components such as the OAPs and the work surface have undergone additional cool cycling between 77 and 293 K. Most of the pieces were machined in the shops of the Cornell physics and engineering departments.

The optical components, including the OAP and flat mirrors and their mounts, the filter and slit wheels, the detector, and the carousel, are mounted on a single 1 inch thick lightweighted aluminum workplate. The aluminum OAPs are bolted directly to their mounts, with fine alignment accomplished using simple shims. Because the thermal contraction of the Zerodur flat mirrors differs from the rest of the optical system, they are held

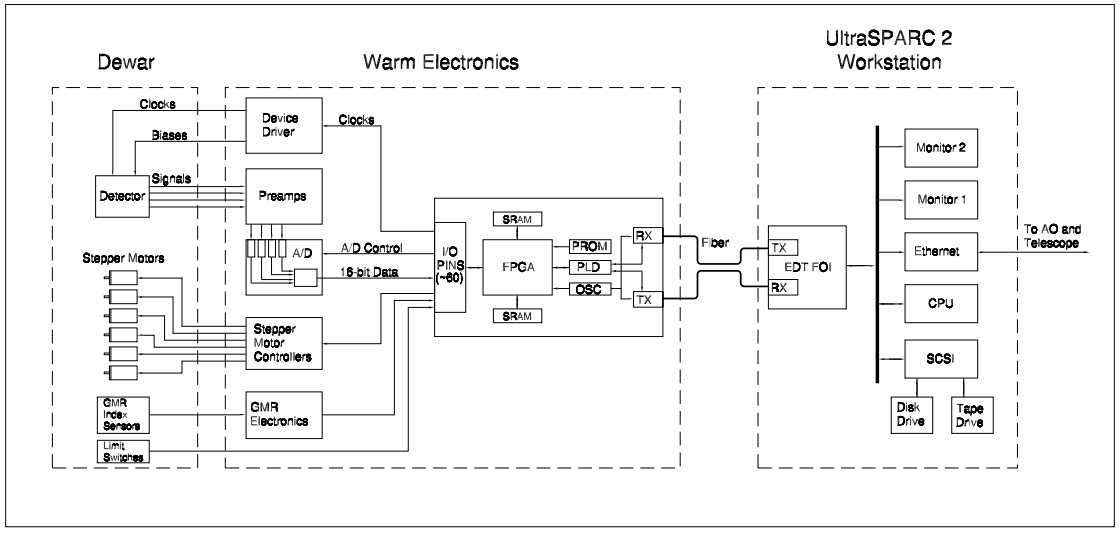

FIG. 5.—PHARO control system

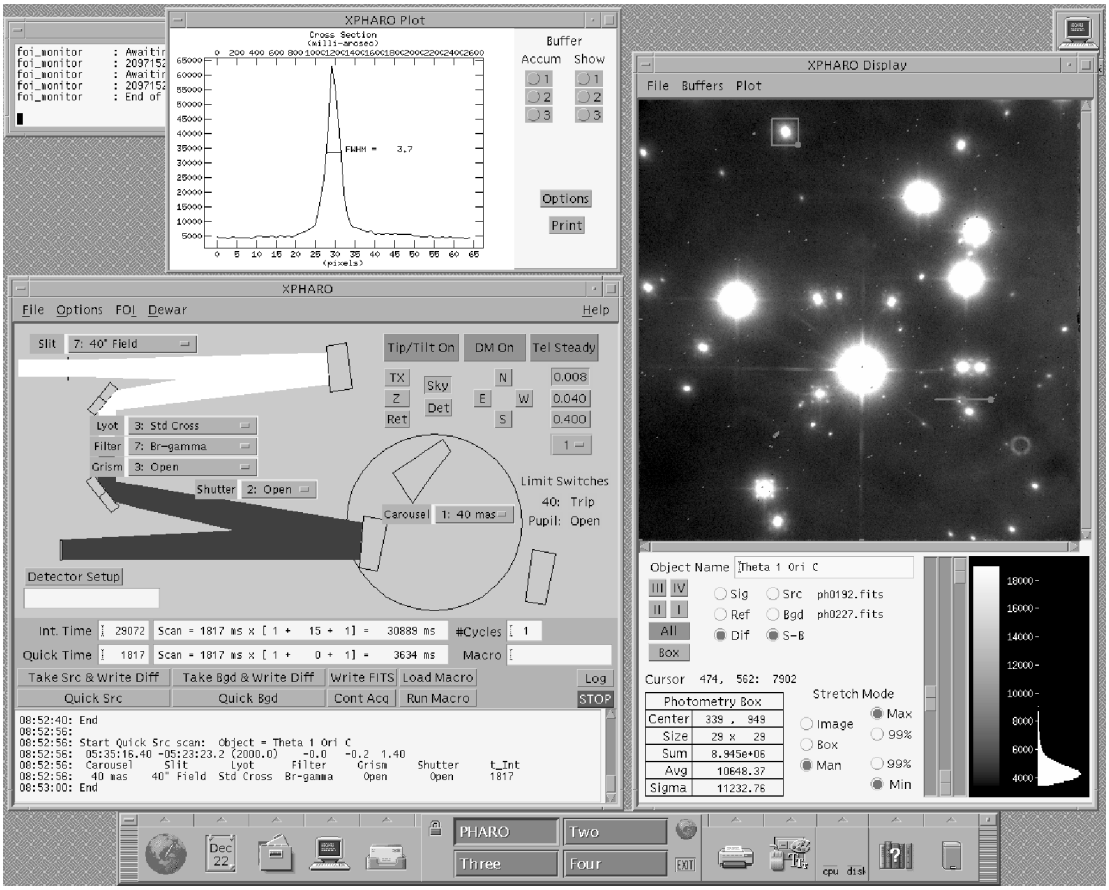

FIG. 6.—XPHARO GUI interface running in the Solaris CDE. The instrument configuration is graphically displayed in the main window at left and is changed by interacting with the embedded buttons, pull-down menus, and text windows. Detector integrations are managed with the controls near the bottom of the main window, and AO system and telescope controls and status displays are provided in the upper right. A separate window at right contains part of the quick-look display where a magnified subsection of the image is displayed; a third window on an additional monitor (not shown) always displays the full 1024 × 1024 image. The display includes simple photometry and plotting tools that permit initial quantitative evaluation of the data.

in (backside) spring-loaded mounts with their surface at the nominal position.

3.2. Stepper Motors and Position Sensors

Because of the large number of moving mechanisms (four 10 position wheels, the carousel, and the shutter blade) and the limited space surrounding the dewar on the AO bench, the mechanisms are driven by stepper motors inside the dewar which are especially built for cryogenic applications by Phytron-Elektronik (Gröbenzell, Germany). We have chosen the models VSS20 for the shutter, VSS33 for the four wheels, and VSS43 for the carousel. The motors have a full step angle of 1.°8 and torques of about 5, 47, and 180 mNm, respectively, at 77 K. All motors are driven through four leads in bipolar half-step mode by Phytron Sincos-L linear drivers which are mounted directly outside the dewar. For details on the cryogenic stepper motors, see B. R. Brandl & L. Keller (2000, in preparation).

Because the motors and mechanisms are entirely contained within the dewar, there is no external mechanical indication of their positions. The pupil imaging mode permits checking of the three wheels and the shutter near the pupil, and the slit wheel can be viewed directly through the dewar window, but we wanted a more convenient way to initialize the wheel positions. We accomplished this by mounting differential bridge giant magnetoresitive (GMR) sensors near each wheel, and small magnetic actuators on each wheel. GMR sensors, manufactured by NVE (Eden Prairie, Minnesota), are metallic thin-film devices which have greater output than conventional anisotropic magnetoresistive (AMR) sensors or Hall effect sensors. When a magnet passes over a differential GMR sensor as a wheel rotates, the change in field triggers a pulse in an external circuit designed by one of us (C. B.) that indicates the wheel is at the index position.

The f/19 and pupil imaging mirrors, both of which are mounted on the carousel, must be locked in precise positions when the instrument is operated in these two modes. The carousel therefore has two hard stops at each end of its travel

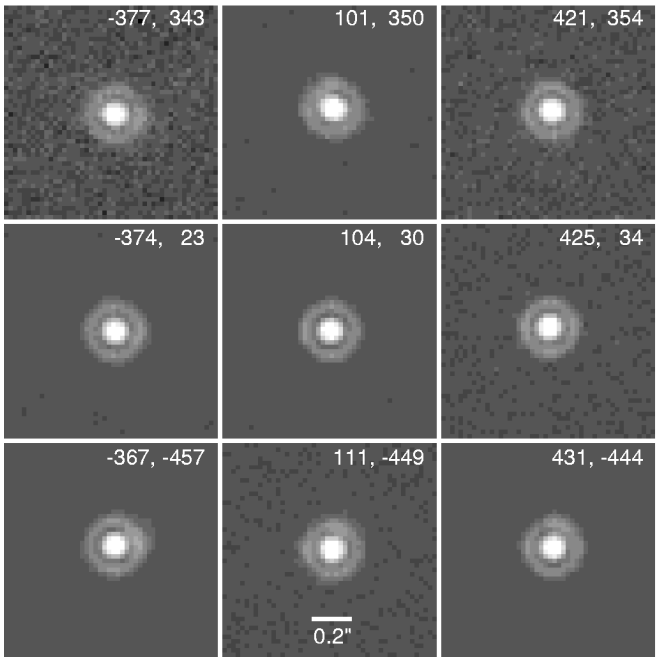

FIG. 7.—Pinhole mask images taken with the *K* filter in f/30 (25 mas pixel^{-1}) mode. Nine pinholes near the center, edges, and corners of the array are shown; each panel is labeled with the offset from the center of the array in pixels. Near the center the peak-to-total flux ratio is 0.053, comparable to the value of ~0.054 expected for a diffraction-limited system.

which are adjusted to stop the carousel at the proper angle. Permanent samarium-cobalt magnets placed in these hard stops pull on a magnetic stainless steel 316 block mounted on the wheel to ensure that the carousel remains firmly against the stop once the motor stops turning. The gearing of the carousel is deliberately designed with sufficient play to permit the magnets to pull the wheel into the stops, and two mechanical limit switches prevent the motor from overdriving the wheel.

3.3. Dewar Construction

The dewar design posed several unusual problems, again because of the limited space on the AO optical bench. The AO optics hang down from the bench, so PHARO too is suspended from this platform. We wanted to keep the camera as close to the bench as possible to avoid flexure introduced by long moment arms, but there was insufficient room above the optical axis for liquid nitrogen (LN_2) vessels, which are commonly mounted above detectors and optics. We therefore decided to place the LN_2 cans below the workplate, which is acceptable in this all-LN_2 system where the detector temperature is not especially critical. Figure 4 shows two views of the PHARO dewar and its internal components. The dewar was manufactured by Precision Cryogenics, Inc., and is made almost entirely of 6061-T6 aluminum. The outer shell wraps tightly around the workplate carrying the optics and is split into an upper and a lower half. The upper half is made of $\frac{3}{8}$ inch (0.95 cm) aluminum plate sides, a $\frac{1}{4}$ inch (0.64 cm) curved top, and a $\frac{3}{4}$ inch (1.9 cm) flange around the bottom and is designed to provide a rigid support for the rest of the dewar. Three stainless steel mounting posts on the upper shell provide attachment points to the AO bench interface. The bottom half of the dewar is composed of a second flange, a lightweight shell, and two separate LN_2 cans. The workplate is connected to the bottom flange with four G-10 fiberglass tabs, and the 3.3 liter inner can is bolted directly to the workplate to provide cooling of the detector and optics. The 11 liter outer can is integrated into a radiation shield which envelopes the workplate. The hold times are ~36 hr for the outer can and ~60 hr for the inner can. The filling necks, vacuum valve, and other fittings protrude from the bottom of the dewar. Insert tubes, or "stingers," screwed into threads at the base of each neck, permit operation with the necks pointing down.

Because minimizing flexure is so important, we contracted Advanced Design Consulting of Lansing, New York, to conduct a finite-element analysis of the dewar shell, the workplate, and the G-10 mounting tabs. This analysis showed that the flexure of the workplate relative to the mounting flange is less than 1 μm through a 45° tilt angle in any direction.

The cabling for the detector and stepper motors runs through three vacuum feedthrough connectors mounted in two access ports in the bottom of the dewar. Because the upper vacuum shell and radiation shield contain no feedthroughs, they can be easily removed, and all interior components can then be accessed without having to disturb mechanical or electrical connections.

4. HAWAII DETECTOR AND ELECTRONICS

PHARO's detector is a science grade, 1024 × 1024 pixel, HAWAII array delivered by the Rockwell Science Center in 1998 May. The array is subdivided into four quadrants, and six clocks and six bias voltages are required for operation. (For a detailed description of HAWAII arrays, see Kozlowski et al. 1994 and Hodapp et al. 1996.) Our device is linear to ~$8 \times 10^4\, e^-$, and the read noise in a correlated double sampling (CDS) read operation is about 9 e^-. The quantum efficiency is above 0.50 over the 1.0–2.5 μm wavelength range and approaches 0.70 in the *K* band. Compared to the NICMOS III 256 × 256 pixel arrays, this detector has a significantly lower readout noise and reduced residual images from previous exposures.

The instrument control system is illustrated in Figure 5. The detector electronics consist of five separate boards. The detector is mounted on a fanout board which contains off-chip field effect transistors (FETs) that are used instead of the on-chip FETs to reduce multiplexer glow (Hodapp et al. 1996). The warm electronics include device driver, preamplifier, and A/D boards purchased from the University of Hawaii Institute for Astronomy, who designed them specifically for operation of the Rockwell HAWAII arrays. The A/D boards are 16 bit,

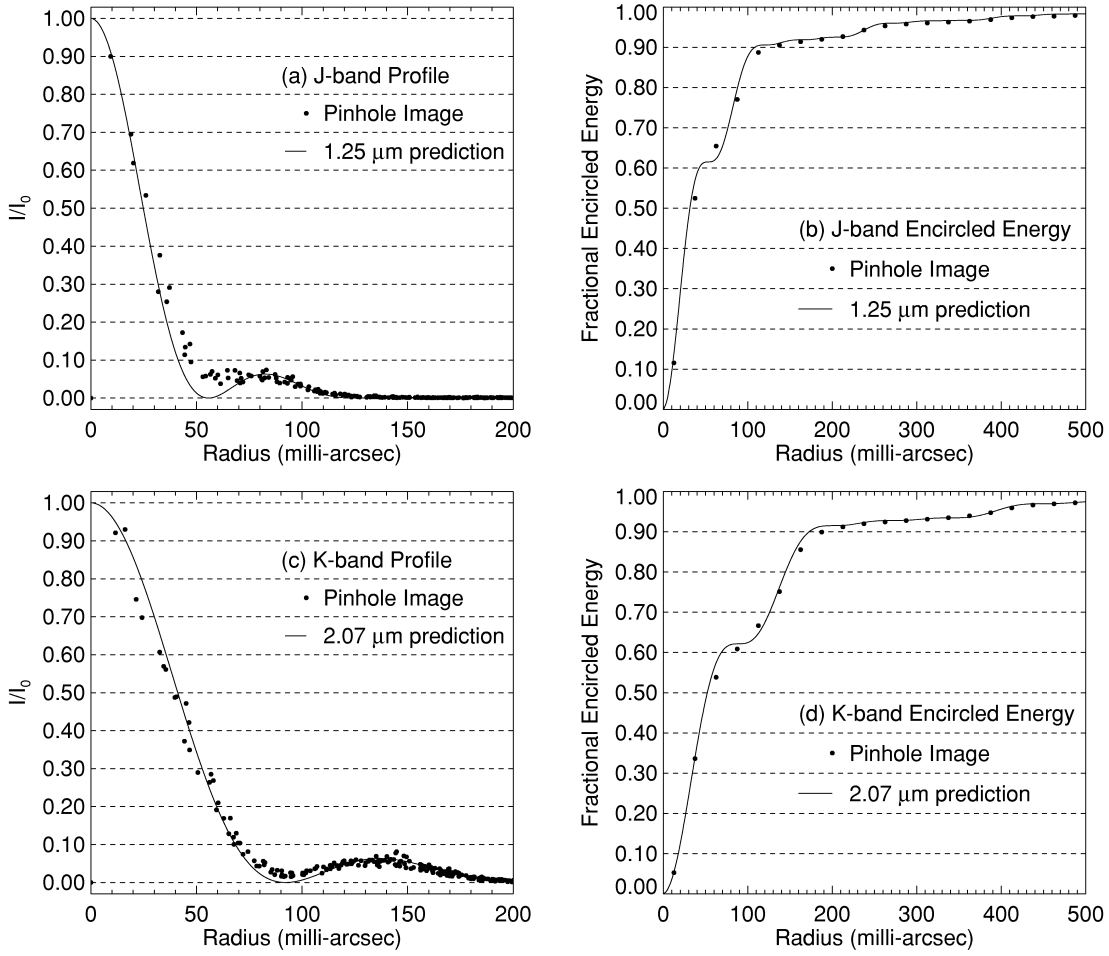

FIG. 8.—Pinhole image measurements compared to theoretical profiles for a 4.978 m clear aperture and a 1.841 m diameter central obscuration (corresponding to PHARO's standard pupil mask). (*a*) Cross section through pinhole image ~200 pixels from the detector center at *J* in the f/30 (25 mas pixel^{-1}) mode. (*b*) Encircled energy function of the same pinhole image at *J*. (*c*) Cross section at *K*, f/30. (*d*) Encircled energy at *K*. The Strehl ratio at both wavelengths is greater than 0.95. The effective wavelength of the *K* data, judged by the peak wavelength of the first ring, appears to be ~2.07 μm instead of the nominal central wavelength of the filter, 2.2 μm. The shift is probably due to the relatively blue light source used to illuminate the pinhole mask.

1 MHz devices, so the detector's entire dynamic range is covered at a single gain setting. The measured electronics system noise is ~1.3 ADUs (<2 e^-), well below the detector read noise.

The fifth board in the detector electronics generates the clock waveforms needed by the detector and stepper motors. The board, which was custom built at Cornell by one of us (B. P.), contains an Altera 10K50 field programmable gate array (FPGA), 8 Mbytes of SRAM memory, and a fiber-optic interface for communications with the workstation. The FPGA provides logic and memory resources which can be reconfigured in-circuit by transmitting a program file from the workstation via the fiber. For hardware interfacing, 160 I/O pins are available. To clock the HAWAII detector, which requires relatively simple waveforms, we have programmed the basic clocking patterns directly into the FPGA logic. Short command packets transmitted to the FPGA via the fiber interface are used to start an integration and specify the integration time, the size of the frame readout, and the number of nondestructive reads per integration. As the detector is read out, data are transmitted to the workstation via the fiber. The logic for driving the stepper motors and sensing home signals from the GMR electronics is also programmed into the FPGA. Therefore, the entire instrument is controlled via the fiber interface. Because the FPGA is programmed after power up either from an on-board EPROM or through the fiber interface, making even major changes to the instrument control protocol is simply a matter of modifying the FPGA software.

5. CONTROL SYSTEM

The PHARO control computer is a Sun UltraSPARC 2 workstation. Although we originally considered utilizing a real-time

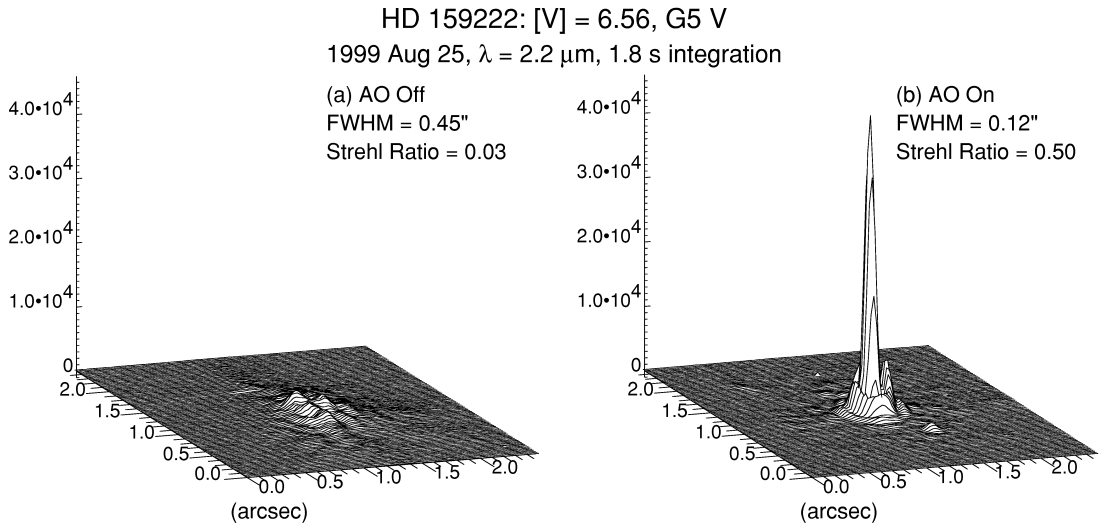

FIG. 9.—Images of HD 159222 taken with the *K* filter at 25 mas pixel^{-1}. (*a*) With the AO system off, the *K*-band seeing was under 0.″5, but the Strehl ratio was only ~0.03. (*b*) With the AO tip-tilt and high-order correction loops closed, the Strehl ratio increased to 0.50 and the FWHM was nearly diffraction limited. A faint ghost visible to the lower right of the star is caused by the 1% neutral density filter which was in place to avoid saturating the detector.

UNIX operating system, we have found that the standard Solaris operating system supplied by Sun functions well for our application. The most time critical functions of the instrument, such as the detector clocking, are executed directly by the FPGA, so the real-time demands on the operating system are not severe. To communicate with the FPGA board via the fiber link, the workstation contains an SCD-FOI S-bus fiber-optic interface (FOI) board manufactured by EDT, Inc. The board's device driver software uses direct memory access (DMA) to the computer's system memory for efficient transfer of large blocks of data. We also added a second video card and monitor to the workstation so that a full 1024 × 1024 pixel image can be displayed on one monitor while the instrument control is managed from the other.

The XPHARO control software is written in C and features a GUI interface that is built with the X-Windows MOTIF libraries and runs in the Solaris Common Desktop Environment (CDE). The GUI interface, shown in Figure 6, includes a graphical display of the positions of the wheels and carousel and the resultant light path inside the dewar, controls for the mechanisms and detector, and basic remote controls for the AO system and telescope. A magnified subsection of the array is displayed on the main monitor, while an image of the full array appears on a second monitor (not shown in Fig. 6). The software includes several buffers so that source and background images, or their difference, can be displayed. Image processing functions such as aperture photometry and plotting are provided to permit real-time analysis of the data.

The FPGA is commanded via small data packets transmitted by the FOI board over the fiber, and image and other data from the FPGA are managed via reads of the FOI device. Because the data reads are blocked (the thread calling the read function stops until the read returns), the XPHARO software is multithreaded. A main thread manages overall user input and data display while a subthread handles the incoming data from the fiber link. This arrangement allows an operator to examine and manipulate an existing image during a long integration. When the integration is complete, the subthread reads the in-

TABLE 8
G45.45+0.06 POINT-SOURCE SENSITIVITY[a]

Filter	Strehl Ratio	ROI Diameter[b] (arcsec)	Fractional Flux[c]	*m* for S/N = 10 in 476 s[d]	*m* for S/N = 10 in 3600 s[d]
J	0.019	0.475	0.29	20.2	21.3
H	0.046	0.475	0.45	19.8	20.9
K′	0.11	0.375	0.36	18.5	19.6

[a] Guiding on the $V \approx 12.3$ star 10″ east of H II region, visible seeing ≈1.″1.
[b] Diameter of region of interest (ROI).
[c] Fraction of star's flux within the ROI.
[d] Half this time is spent on the source, the other half on the sky.

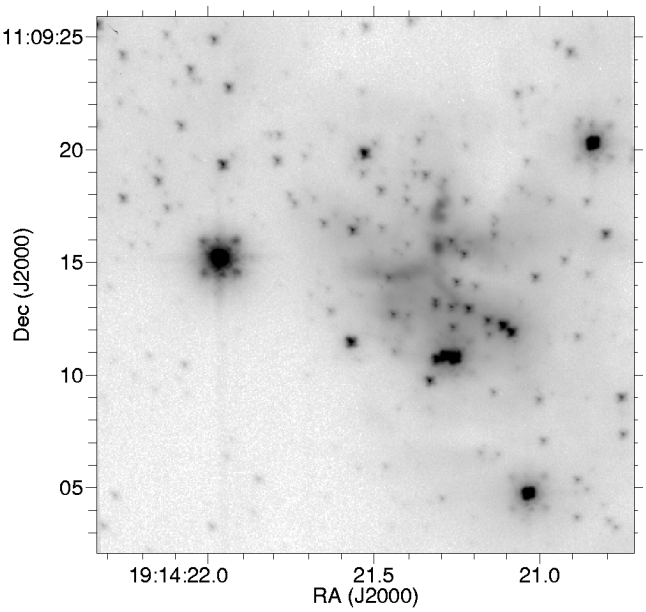

FIG. 10.—Image of the ultracompact H II region G45.45+0.06 at K' taken on 2000 May 13 in the 25 mas pixel^{-1} mode. The image is a combination of two 119 s H II region images and two 119 s background images. The AO guide star ($V \approx 12.3$) is the brightest object about 10″ east of the H II region. The *K*-band seeing during the observations was 0.″8, the Strehl ratio is 0.11, and sources as faint as $K' \approx 18.5$ are visible.

coming data into memory, then passes a signal to the main thread to write data to disk and update the display as desired.

Image data are written to disk in standard FITS format. The workstation includes a 9 Gbyte disk and an 8/14 GByte capacity Exabyte tape drive for data storage and backup.

6. INSTRUMENT PERFORMANCE

6.1. Image Quality

PHARO's intrinsic image quality can be evaluated using the pinhole grid mask that is mounted in the slit wheel. Figure 7 shows *K*-band, 25 mas pixel^{-1} images of nine pinholes distributed across the detector. Figure 8 compares the radial profiles and encircled energy functions of two pinhole images at *J* and *K* to theoretical profiles. The Strehl ratios of these pinhole images are greater than 0.95 across the array at both wavelengths.

6.2. AO Imaging

Figure 9 displays surface plots of two PHARO *K*-band images of the $V = 6.5$ star HD 159222 with the Palomar AO correction loop open and closed. The open-loop Strehl ratio is only 0.03, and the seeing at *K* was under 0.″5. The closed-loop Strehl ratio is 0.50, and the image core is nearly diffraction limited.

A closed-loop image of the ultracompact H II region G45.45+0.06 at K' is shown in Figure 10. This object is a frequent target for AO systems (e.g., Feldt et al. 1998) because a suitable guide star ($V \approx 12.3$) lies about 10″ east of the nebula. This star is the brightest object visible in Figure 10. Surrounding it and a few other bright stars is a four-point spot pattern caused by "waffle mode" (aliasing) of the AO system's deformable mirror. In this image, the spots are about 1% of the primary image in brightness. Care must be taken not to confuse these spots with real sources, but this is straightforward because the spots always lie at the same offsets relative to the star.

TABLE 9
BRIGHT GUIDE STAR POINT-SOURCE SENSITIVITY[a]

Filter	Strehl Ratio	ROI Diameter[b] (arcsec)	Fractional Flux[c]	*m* for S/N = 10 in 3600 s[d]
J	0.062	0.275	0.31	22.0
H	0.14	0.250	0.31	21.7
K′	0.33	0.225	0.32	20.5

[a] Guiding on 47 UMa, $V \approx 5.1$, visible seeing ≈1.″1.
[b] Diameter of region of interest (ROI).
[c] Fraction of star's flux within the ROI.
[d] Half this time is spent on the source, the other half on the sky.

The G45.45+0.06 K' image, and two others at *J* and *H*, were calibrated against the photometric standard star AS 31-0 (Hunt et al. 1998). The photometric properties and sensitivities of the images are presented in Table 8. The point-source sensitivity is dependent on several factors, including the seeing at the time of the observation (~ 1″ in the visible, which is about average for Palomar) and the brightness of the guide star. The $V \sim 12.3$ guide star for this object is near the faint limit for the Palomar AO system, especially for good correction at *J* and *H*.

In addition to the nebulosity of the H II region itself, Figure 10 shows the accompanying star cluster, with a limiting magnitude $K' \approx 19$. Because the complex lies behind many magnitudes of obscuring dust, it cannot be seen at visible wavelengths, and near-infrared AO imaging provides the only means of measuring the number, luminosity distribution, and extinction of the cluster members.

Measured point-source sensitivities while guiding on 47 UMa ($V = 5.1$), also calibrated against AS 31-0, are presented in Table 9. The Strehl ratios are 3 times higher and the sensitivity about 0.7 mag fainter than for the H II region data, owing to the brighter guide star. The sensitivity is dependent on the transmissivity of the optical system, which includes 11 warm reflective surfaces in the telescope and AO system. The observed signal levels of photometric standards indicate a warm optics transmissivity of about 45%, or 93% per surface.

6.3. Coronagraph Mode Performance

The performance of the Palomar AO system together with PHARO's coronagraphic masks and Lyot stops has been extensively described by Oppenheimer et al. (2000). The effectiveness of the coronagraphic masks and pupil stops can be characterized by the dynamic range (the ratio of the primary star intensity to the faintest detectable point-source intensity)

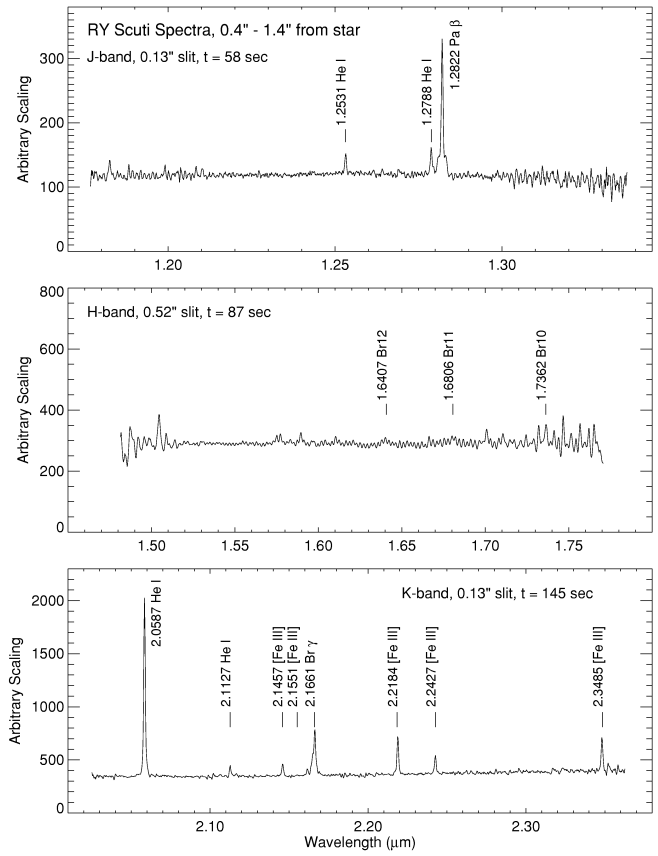

FIG. 11.—Ratio spectra of the nebulosity surrounding RY Scuti divided by the star HR 509. Two zones on both sides of the star between 0.″4 and 1.″4 distance from the star were averaged to produce the plotted spectra. Recombination lines of H and He are visible as well as several forbidden lines of [Fe III].

as a function of radius from the primary. In the *K* band, the best coronagraphic performance is achieved with the large spot (0.″97 diameter, or 11 Airy rings) and the "large" Lyot stop, where the dynamic range varies from 8 to 12 mag between 1″ and 2.″5 radius from a star of $K = 4.71$ when the Strehl ratio is ~0.5. Outside 2.″5 the dynamic range is limited by the (background limited) sensitivity of the system. At *J*, Oppenheimer et al. (2000) predict that the 0.″43 spot and the "medium" Lyot stop will result in the maximum dynamic range. The dynamic range of course depends on the Strehl ratio, which in turn depends on the brightness of the guide star and quality of the seeing.

6.4. AO Long-Slit Spectroscopy

To demonstrate PHARO's spectroscopic capabilities, we present spectra of RY Scuti, an eclipsing, "overcontact" close binary star embedded in an ~1″ × 2″ nebula (Gehrz et al. 1995; Smith et al. 1999). The system's optical spectrum has long been known to be peculiar, with prominent [Fe III] lines (e.g., Cowley & Hutchings 1976). RY Scuti is an attractive target for AO because of the nebula's small size and the presence of

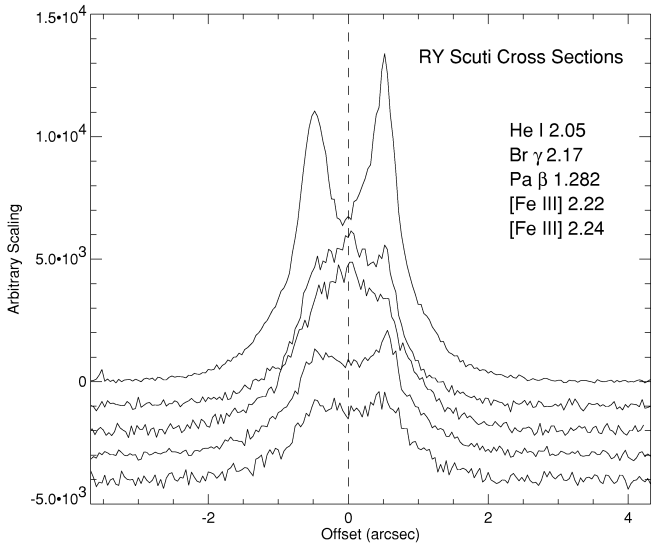

FIG. 12.—Spatial cross sections through the RY Scuti nebula in five spectral lines. The profiles have been offset from each other vertically for clarity.

a suitable guide star ($m_V = 9.08$) at its center. Locking on the central star, the Palomar AO system achieved a Strehl ratio of 0.12. We oriented our slit along the nebula's long axis (at position angle 56°) and took *J*, *H*, and *K* spectra through the 0.″13 and 0.″52 slits.

The RY Scuti spectra were divided by spectra of the star HR 509 to remove telluric and instrumental signatures. The mean ratio spectra of both sides of the nebula between 0.″4 and 1.″4 distance from the star are plotted in Figure 11. Several spectral lines in the *J* and *K* bands are detected, from recombination lines of H and He to forbidden lines of [Fe III] reminiscent of the optical spectra. To our knowledge this is the first detection of the infrared [Fe III] lines in this object. The lines in the *J* and *K* bands are 3.5–4.0 pixels FWHM, as expected for the 0.″13 slit (3.25 pixels wide at 40 mas pixel^{-1}). The resolving powers are $R = 2030$ at 1.282 μm Paβ and $R = 1720$ at 2.059 μm He I (see Table 6).

Because these are long-slit spectra, we can also examine the spatial variation in line intensity along the length of the slit. The spatial profiles through the long axis of the nebula in the five brightest emission lines are displayed in Figure 12. The mean stellar continuum profile on the blue and red sides of each line was subtracted from the line profile to remove the star's contamination. We detect distinct differences in the spatial profiles of the different lines: the He I line is double-peaked, the H lines are more flat-topped, and the [Fe III] lines have an intermediate shape. The variations between the profiles appear to indicate different ionization zones within the nebula.

The PHARO project was funded by the National Science Foundation's Academic Research Infrastructure Program grant AST 96-01507, the Norris Foundation, and the Cornell University Department of Astronomy. We are grateful to the many

suppliers of the excellent components in our instrument. Craig Cabelli at the Rockwell Science Center provided valuable advice on the HAWAII detector, Klaus Hodapp and Ev Irwin at the University of Hawaii built a set of their proven array electronics boards for us and lent crucial advice on how to use them, and Dick Gummer at Precision Cryogenics assisted with the dewar design as well as executing its actual construction. Mark Mason and Jerry Gaffke at EDT, Inc., lent advice on their fiber-optics board. Altera Corp. provided support under their Altera University Program. We extend special thanks to the members of the Cornell University machine shops in both the physics and engineering departments who manufactured many of the mechanical components inside the dewar—the nearly perfect optical and mechanical alignments we obtained the first time the optical bench was assembled were a direct result of their skill. We are very grateful to the members of the Palomar AO project at JPL for the opportunity to build an instrument for their excellent AO system and to the staff of Palomar Observatory for valuable assistance with the commissioning and operation of PHARO at the telescope.

REFERENCES

Bloemhof, E. E., & Dekany, R. G. 1998, Proc. SPIE, 3353, 638
———. 1999, in ASP Conf. Ser. 174, Catching the Perfect Wave: Adaptive Optics and Interferometry in the 21st Century, a Symposium Held as Part of the 110th Annual Meeting of the ASP, ed. R. Restaino, W. Junor, & N. Duric (San Francisco: ASP), 69
Born, M., & Wolf, E. 1980, Principles of Optics (6th ed.; Oxford: Pergamon)
Brandl, B. R., Hayward, T. L., Houck, J. R., Gull, G. E., Pirger, B., & Schoenwald, J. 1997, Proc. SPIE, 3126, 515
Cowley, A. P., & Hutchings, J. B. 1976, PASP, 88, 456
Dekany, R. E., Brack, G., Palmer, D., Oppenheimer, B. R., Hayward, T. L., & Brandl, B. 1998, Proc. SPIE, 3353, 56
Feldt, M., Stecklum, B., Henning, T., Hayward, T. L., Lehmann, T., & Klein, R. 1998, A&A, 339, 759
Gehrz, R. D., et al. 1995, ApJ, 439, 417
Hardy, J. W. 1998, Adaptive Optics for Astronomical Telescopes (New York: Oxford Univ. Press)
Hodapp, K.-W., et al. 1996, NewA, 1, 177
Hunt, L. K., Manucci, F., Testi, L., Migliorini, S., Stanga, R. M., Baffa, C., Lisi, F., & Vanzi, L. 1998, AJ, 115, 2594
Kozlowski, L. J., et al. 1994, Proc. SPIE, 2268, 353
Marshall, J. A., Troy, M., Dekany, R., & Dekens, F. G. 2000, Proc. SPIE, 4007, 741
Oppenheimer, B. R., Dekany, R. G., Hayward, T. L., Brandl, B., Troy, M., & Bloemhof, E. E. 2000, Proc. SPIE, 4007, 899
Roddier, F. 1999, Adaptive Optics in Astronomy (Cambridge: Cambridge Univ. Press)
Schroeder, D. J. 2000, Astronomical Optics (San Diego: Academic)
Smith, N., Gehrz, R. D., Humphreys, R. M., Davidson, K., Jones, T. J., & Krautter, J. 1999, AJ, 118, 960
Troy, M., et al. 2000, Proc. SPIE, 4007, 31
Tyson, R. K. 1998, Principles of Adaptive Optics (San Diego: Academic)